Supporting Information for:

Self-assembly of metal ions induced highly emissive fluorophore-triphenylamine nanostructures: enhanced two-photon action cross section for bioimaging applications

Lin Kong, Yu-peng Tian*, Qi-yu Chen, Qiong Zhang, Hui Wang, Dong-qin Tan, Zhao-ming Xue, Hong-ping Zhou, Jie-ying Wu, Jia-xiang Yang*

Contents:

1. Crystal structure of **L** including selected bond length and bond angles; The 1D and 2D framework diagram;

2. Morphology of **L** nanostructure obtained from different concentration and/or solvent;

3. XRD patterns of **L** at different states.

4. UV-Vis absorption and fluorescence spectra of **L** at different states.

5. FT-IR spectra

6. SEM images of $Cu(NO_3)_2$ and $Cd(NO_3)_2$

7. Determination of metal ions embedded in **L** matrix;

8. TD-DFT calculation;

9. Photostability and thermal stability

10. Non-linear optical meansurments

11. The average size of the particles used in bioimage and the corresponding concertration

12. 1PFM and 2PFM images

Table S1. Crystal data and structure refinement for **L**

Formula	$C_{29}H_{22}N_2$	Crystal system	Triclinic
Formula weight	398.49	Space group	$P\bar{1}$
T (k)	296(2)	α/ deg	106.347(2)
β/ deg	95.623(2)	γ/ deg	102.023(2)
a/Å	10.2279(12)	b/ Å	11.9024(14)
c/Å	19.510(2)	Z	4
V/Å³	2197.9(4)	Crystal size/ mm	0.24×0.23×0.21
Calculated density (mg/m³)	1.204	F (000)	840
Reflection collected	4126	Goodness of fit on F^2	1.017
R indices (all data)	$R_1 = 0.0994$ $wR_2 = 0.1490$	Final R indices [I>2σ(I)]	$R_1 = 0.0567$ $wR_2 = 0.11$

In the molecule, the bond lengths of the benzene ring and triphenylamine unit were all of aromatic character. The linkage bond length between the benzene ring and the triphenylamine unit was quite conjugated with C16-C19 being 1.457(3) Å and C28-C29 being 1.432(4) Å, which were located between the normal C=C double bond (1.34 Å) and C-C single bond (1.54 Å). The C19=C20 double bond was nearly coplanar to the adjacent benzene and triphenylamine unit with the torsion angle of C17-C16-C19-C20 being 17.6(4)° and C19-C20-C21-C22 being -1.0(4)° as shown in **Fig. 2**. Moreover, the bond angle of N3-C29-C28 was 178.9(4)º with torsion angle of C24-C27-C28-C29 being -179.6(3)º, that was to say, the C≡N unit was a perfect linear group which formed a π-delocalization unit along the benzene ring and C=C double bond chain. The structural features suggested that all nonhydrogen atoms were highly conjugated and nearly coplanar, which was contribute to the electronic delocalization in the whole molecule.
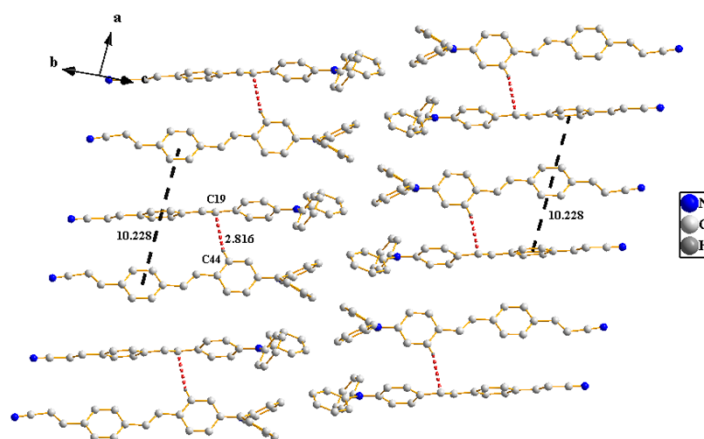
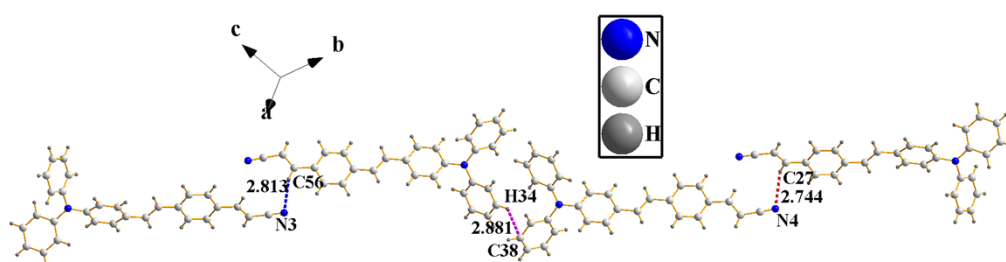**Figure S1** The 1D framework along *a* axis shown C-H···π interaction and π···π interaction

Figure S2 The 1D framework shown C-H···C interaction and C-H···N interactions
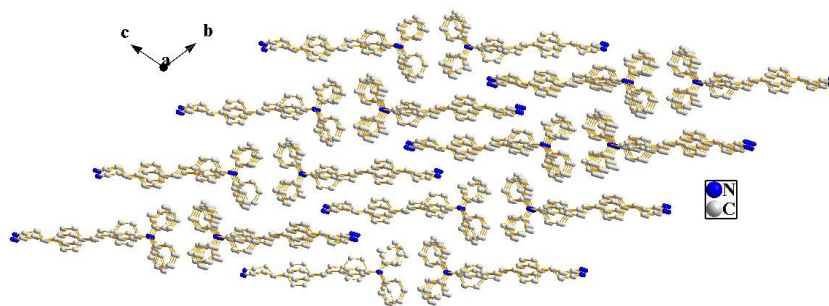
Figure S3 The 2D architecture along *bc* plane

Table S2. Bond lengths [Å] and angles [°] for **L**

|					
C(1)-C(2)	1.380(3)	N(1)–C(1)	1.420(3)	C(7)–N(1)	1.424(3)
C(13)-N(1)	1.407(3)	C(16)-C(19)	1.457(3)	C(19)-C(20)	1.327(3)
C(29)-N(3)	1.127(3)	C(27)-C(28)	1.288(3)	C(28)-C(29)	1.432(4)
C(24)-C(27)	1.459(4)	C(20)-C(21)	1.448(3)	C(2)-H(2)	0.9300
C(13)-N(1)-C(1)	122.82(19)	C(13)-N(1)-C(7)	117.89(17)	C(1)-N(1)-C(7)	119.28(19)
N(1)-C(13)-C(14)	123.8(2)	C(15)-C(16)-C(19)	121.6(2)	C(16)-C(19)-C(20)	126.0(2)
C(23)-C(24)-C(27)	124.0(2)	C(24)-C(27)-C(28)	129.0(3)	C(19)-C(20)-C(21)	129.6(2)
C(27)-C(28)-C(29)	122.4(3)	C(28)-C(29)-N(3)	178.9(4)		

Morphology of L nanostructure

   L nanostructures were simply prepared from mixed solution of tetrahydrofuran (THF)-water, ethanol (EtOH)-water and/or N,N-dimethylformamide (DMF)-water without addition of any template, catalyst and/or surfactant. SEM images of self-assembly aggregations of **L** from EtOH-H_2O solution are shown in **Fig. 1b** and **S4**. The influence of concentration on the morphology was also studied. When the concentration was as low as 1.0×10^{-5} mol·L^{-1}, a regular square structure with the angle being close to 90 º was presented as shown in **Fig. 1b**. The side length of the square was about 400 nm. When the concentration increased to 2.0×10^{-5} mol·L^{-1}, the as-formed regular square began to bend, and some hemispherical-like structures were appeared with the diameter of about 400 nm (**Fig. S4b**). Then, two hemispheres grew together to form a structure similar to the shape of a peanut shell. The junction part of the two hemispheres was recessed, which could be observed very clearly. As the concentration was further increased to 3.5×10^{-5} mol·L^{-1}, the recessed and bended peanut shell aggregated and the degree of such a recess and bending was more deepened (**Fig. S4c**). Further, when the concentration was up to 4.0×10^{-5} mol·L^{-1}, the aggregated structure showed the morphology of rose petals, swaying in the wind (**Fig. S4d**).

   The morphologies of **L** prepared from DMF-H_2O mixed solution showed bending of nanobelts with 2~3 μm long and 150~200 nm wide (**Fig. S5**). The morphologies of **L** obtained from THF-H_2O also had the characteristics of the bend. The as-prepared bended nanofibres had the length of 10~15 μm as shown in **Fig. S6**. The results clearly revealed the difference between **L-L** interactions and **L**-solvent interactions. It is known that the morphology of organic nano- and submicro-structure is determined by different dominant intermolecular interactions, such as H-bonds, π-π interactions and van der Waals force etc. When the concentration was low, the noncovalent intermolecular interactions of **L**-solvent were stronger than those of **L-L**, resulting in particles with a smaller size. On the contrary, as the concentration increases, the interactions of **L-L** will be stronger than that of **L**-solvent. Thus, **L** molecules tend to aggregate, resulting in particles with a larger size. And, the bended morphology observed here clearly revealed the intermediate state of the aggregation.
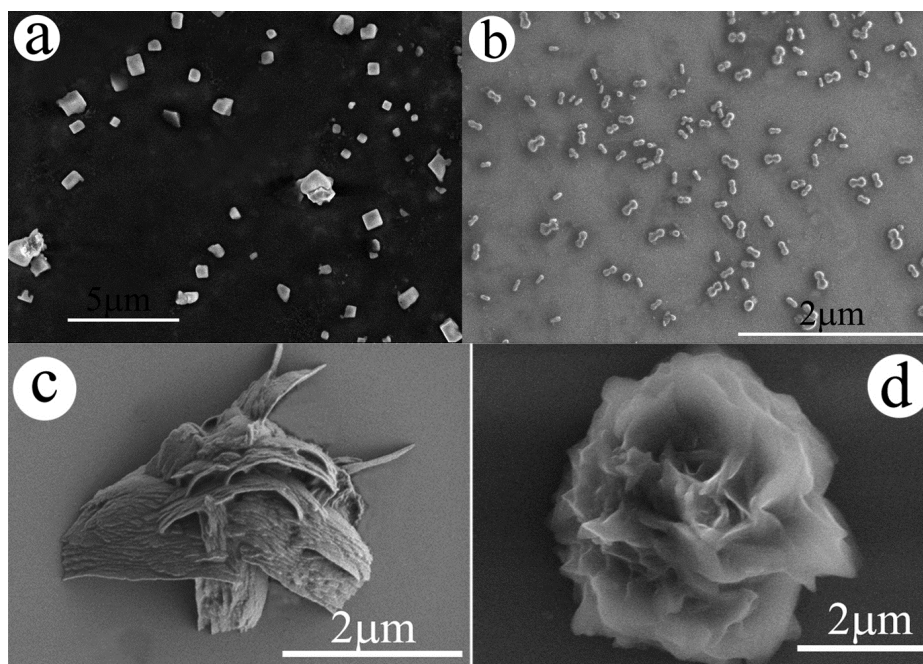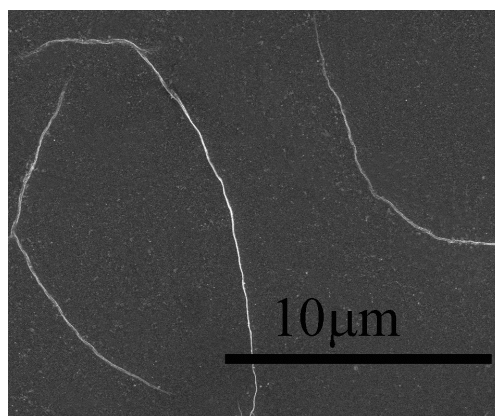
Figure S4 SEM images of **L** obtained from EtOH-H$_2$O solution with different concentrations:
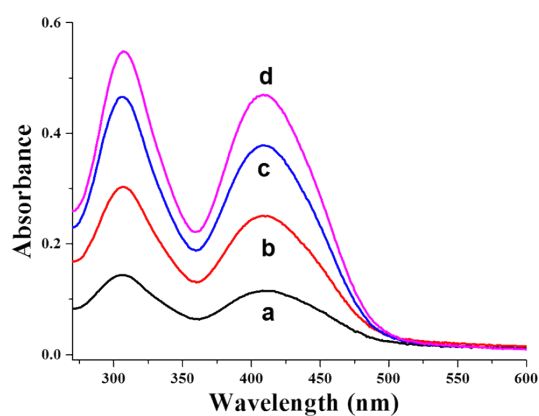
(a) 1.0×10^{-5} mol·L^{-1}; (b) 2.0×10^{-5} mol·L^{-1}; (c) 3.5×10^{-5} mol·L^{-1}; (d) 4.0×10^{-5} mol·L^{-1}
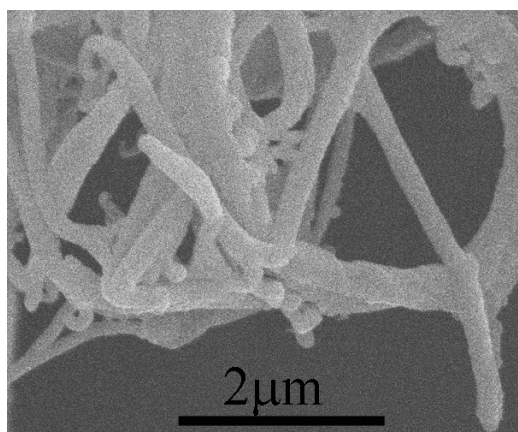
Figure S5 SEM image of **L** obtained from DMF-H$_2$O solution
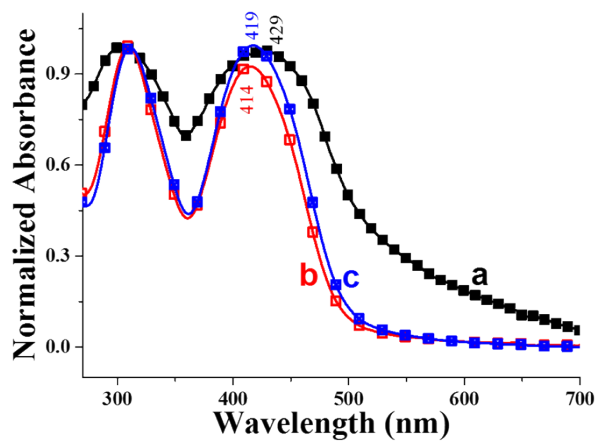

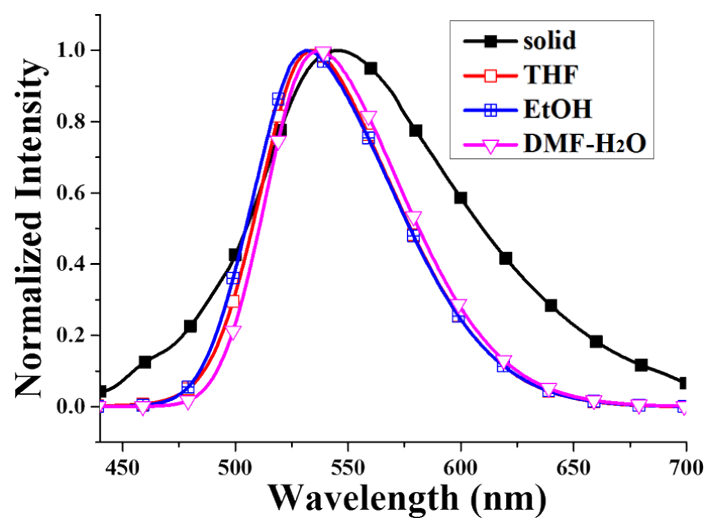**Figure S6** SEM image of **L** obtained from THF-H$_2$O solution

Figure S7 UV-vis spectra of **L** obtained from EtOH-H$_2$O solution with different concentrations:

(a) 1.0× 10^{-5} mol·L^{-1}; (b) 2.0 × 10^{-5} mol·L^{-1}; (c) 3.5 × 10^{-5} mol·L^{-1}; (d) 4.0× 10^{-5} mol·L^{-1}

Figure S8 UV-Vis spectra of **L** a) in solid state; b)-c) **L** nanostructures obtained from b) tetrahydrofuran (THF), c) N,N-dimethyl formamide (DMF) solutions.

Figure S9 Fluorescence spectra of **L** in solid state and **L** nanostructures obtained from EtOH, THF and DMF solutions.

UV-vis absorbance and fluorescence of L nanostructures obtained from different solution

The electronic spectra of **L** nanostructures have been studied at room temperature and the results are shown in **Fig. S7-8**. The dilute **L** solution of ethanol shows two major absorption bands centers at 304 nm and 402 nm, respectively (**Fig. 1b**), the latter corresponds to π-π* transition of the whole π conjugated system, while the former corresponds to π-π* transition of triphenylamine fragment. Meanwhile, the two major absorption bands center at about 304 nm and 429 nm, respectively, in solid state (**Fig. S8a**). Moreover, **L** nanostructures with different morphologies exhibit obviously different absorption spectral profiles (**Fig. S8 and Fig. 1b**). Compared with that of dilute solution, the maximal absorption band of the nanostructures from ethanol, THF and DMF solutions exhibit red-shifts by 18 nm, 12 nm, and 17 nm from 402 nm to 420 nm (**Fig. 4a**), 414 nm (**Fig. S8b**) and 419 nm (**Fig. S8c**), respectively.

Similar to that of UV-vis absorption, **L** molecules at different states exhibit obviously different emission spectral profiles (**Fig. S9**).The dilute **L**-ethanol solution shows yellow emission which centers at 590 nm (**Fig. 1c**), while it shows green emission which centers at about 546 nm in solid state. The maximal emission band of **L** nanostructure prepared from EtOH solution centers at 560 nm (**Fig. 4b**), which is 557 nm for that from THF and 565 nm for that obtained from DMF solution.

The phenomenon of tunable linear optical properties should be attributed to interactions between neighboring molecules. Nanomaterials with different morphologies are promising to exhibit different optical properties due to different ways of molecular stacking. The different interactions between **L-L** molecules and **L**-solvent (that is to say the solvent effect) also influence the optical properties.

XRD pattern of L at different states
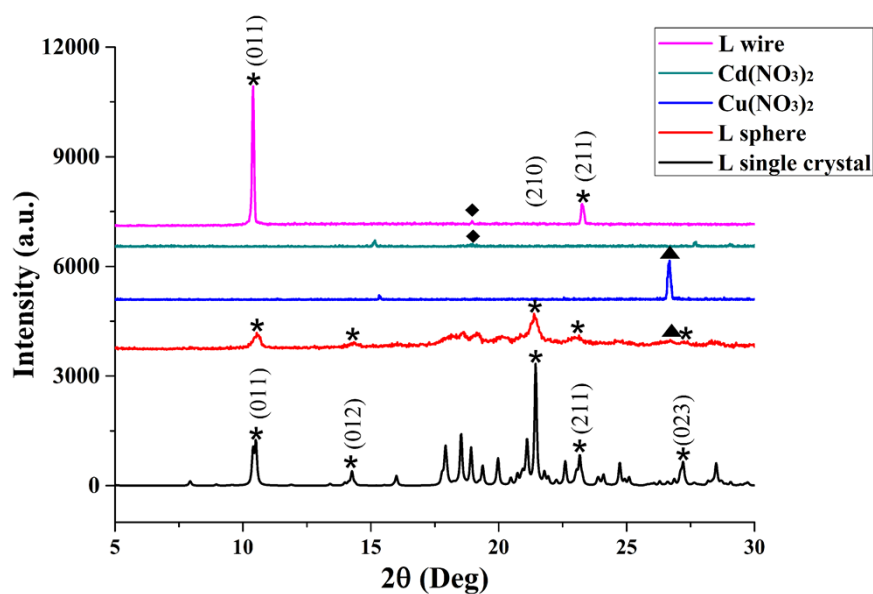
Figure S10 XRD pattern of $Cu(NO_3)_2 \cdot 3H_2O$, $Cd(NO_3)_2 \cdot 4H_2O$ and L at different states

The crystal structure of the products is studied by measuring their XRD patterns. The single crystal and nanoscale crystals of **L** wire/sphere display identical X-ray patterns. The XRD patterns with 2θ near 10.4 ° are similar. Trace impurities such as $Cu(NO_3)_2$ and/or $Cd(NO_3)_2$ was also observed for wire and sphere, respectively, which was marked as triangle and rhomb, respectively. The results suggest that the main component of wire/sphere samples is **L** and that the interactions between **L** and metal ions are weak electrostatic attraction, not strong covalent bond. Furthermore, some minor differences can also be observed. As for wires, the main diffraction peaks at 10.4 ° and 23.2° correspond to the (01l) and (211) reflections. The result is consistent with the wire-like morphology of **L** wire. The sharpness and strong intensity of the diffraction peaks is indicative of high crystallinity of **L** molecules at this state. While for **L** sphere, except for the diffraction peaks at 10.4 ° and 23.2°, some other peaks are also observed, such as 14.3°, 21.4°, 27.2 ° (identified as (012), (210) and (023) reflections), which fits with the spherical morphology of **L** sphere. The results also revealed that the molecular packing differences between the bulk crystal, wires and spheres indeed exist, which results from the participation of metal ions and will results in the tunable optical properties of the samples [S1].
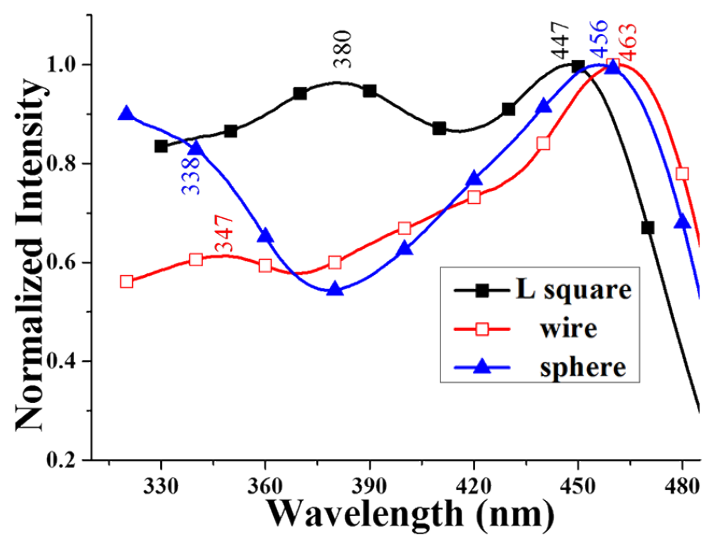
8

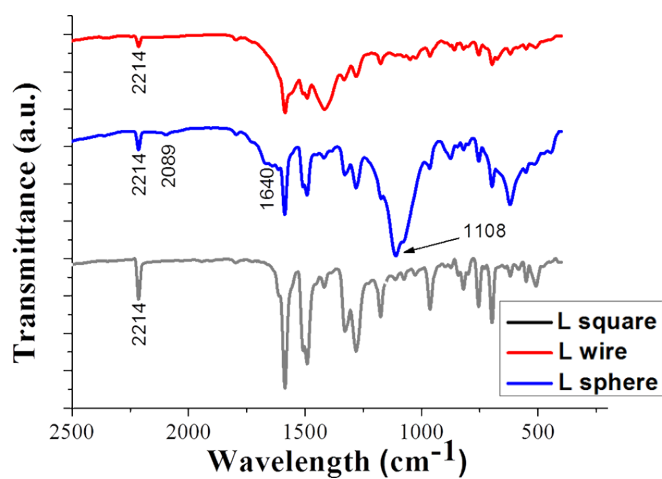**Figure S11** The excitation spectra of **L** squares, wires and spheres

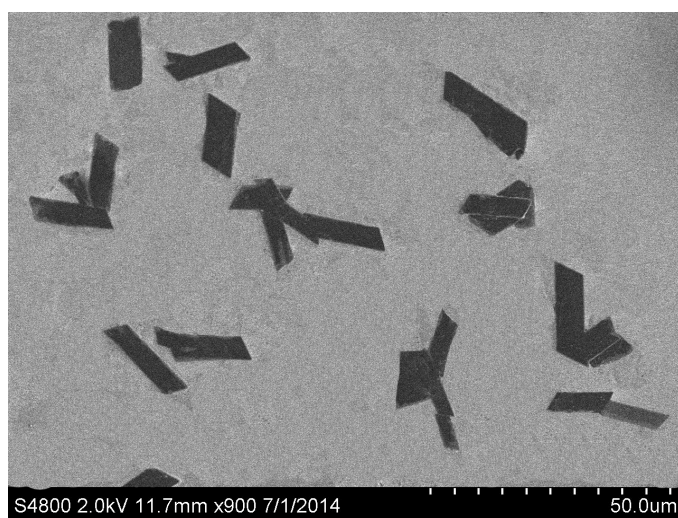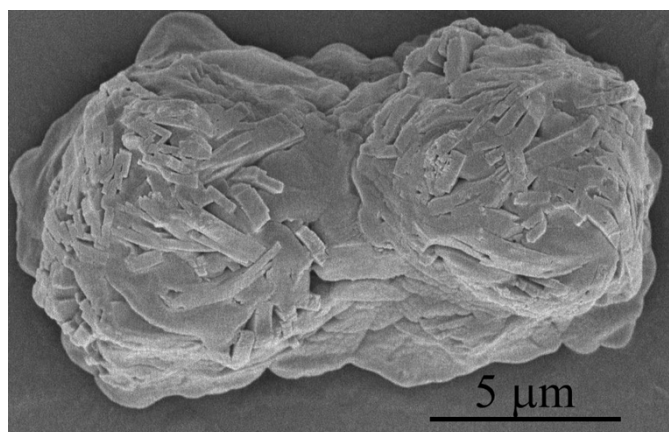**Figure S12** FT-IR spectra of **L** squares, wires and spheres.

**Figure S13** SEM image of Cd(NO$_3$)$_2$ prepared from ethanol-water mixed solution

9

Figure S14 SEM image of $Cu(NO_3)_2$ prepared from ethanol-water mixed solution

Preparation of L-CdS and L-CuS nanohybrids

Further studies revealed that Cd^{2+}, Cu^{2+}, in the form of ions, were embedded in **L** wires and **L** spheres, respectively. The as-prepared **L** wires and/or **L** spheres were placed onto a polished silicon wafer and/or a copper grid, placed undisturbed to remove the solvents, resulting in a light yellow product. The product was washed with high-purity water to remove excessive inorganic residue, and then placed in a desiccator containing acidified Na_2S solution [S2]. Slow reaction of **L** wires and/or **L** spheres with excess H_2S gas occurred for about 12 hours. In this process, the Cd^{2+} ions embedded in **L** nanowires subsequently reacted with S^{2-} to form CdS nuclei, and finally grew into the CdS nanodots all over **L** wires. At the end of the process, the color of the final product in the desiccator turned from light yellow to bright yellow. The color change suggested the formation of the CdS nanodots. **Figure S15a** showed a SEM image for the as-formed **L**-CdS nanohybrid. **Figure S15b** showed the enlarged high-resolution TEM (HRTEM) image. The as-formed CdS nanodots were clearly seen as dark dots in the TEM image. The HRTEM image of the individual CdS nanodots (**Figure S15b**) showed the lattice fringe of about 0.33 nm, corresponding to the (111) plane of the face-centered cubic (FCC) CdS (JCPDS card: 10-454) [S2].

Similar to that occurred in **L** wires, the Cu^{2+} ions were also embedded in the lattice of **L** sphere, which was determined through placed it in an atmosphere of H_2S as discussed above. The color of the final product in the desiccators after 12 h turned from light yellow to black, suggesting the formation of the CuS nanoparticle. The morphology of the as-prepared **L**-CuS nanohybrids was shown in **Figure S15c** to **d**. The surface of **L**-CuS nanohybrids was very smooth and no particles could be observed out of the sphere, which revealed that Cu^{2+} ions were embedded in the lattice of L sphere. Moreover, HRTEM image (**Figure S15d**) showed very uniform lattice fringe of CuS. The lattice fringe was about 0.32 nm, corresponding to the (110) plane of hexagonal CuS (JCPDS card: 78–2121). [S3]

10
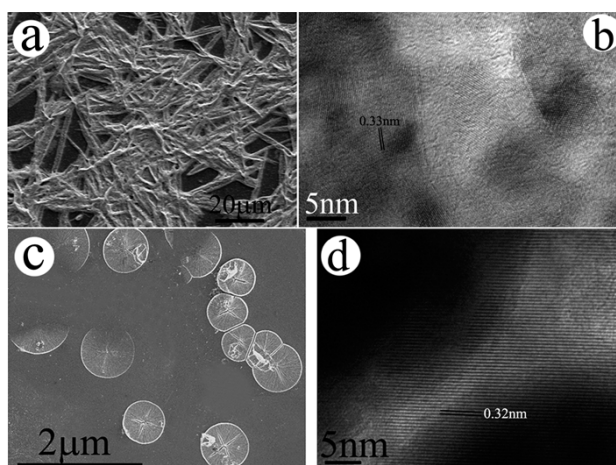
Figure S15 SEM images of (a) **L**-CdS wires, (b) HRTEM image of CdS particles imbedded in the **L**-CdS, (c) **L**-CuS spheres, (b) HRTEM image of CuS particles imbedded in the **L**-CuS;

TD-DFT calculation

The UV-vis absorption spectrum of **L**-ethanol solution exhibited two major absorption peaks at 304 nm and 402 nm (**Fig. 1b**). The latter corresponded to the π-π* transition of the whole π-conjugated **L** molecule, while the former resulted from the π-π* transition of triphenylamine fragment.

To better understand the electronic structure and linear optical properties of **L**, molecular orbital calculations of time-dependent density functional theory (TD-DFT) at the B3LYP-/6-31G(d,p) level basis set [S4] were performed. The molecular geometry used for the calculation was obtained from X-ray diffraction crystallographic data. The orbital features of **L** calculated from TD-DFT method was presented in **Fig. S16**. In the highest occupied molecular orbital (HOMO), the electrons were mainly concentrated on the electron-donor unit (triphenylamine group), while in the lowest unoccupied molecular orbital (LUMO), the electrons mainly concentrated on electron-acceptor unit (cyano unit). Obviously, the electron transition from the HOMO to the LUMO was accompanied by charge transfer from the electron-donor unit to the electron-acceptor unit, which is a typical property of an ICT molecule [S5]. The theoretical spectral characteristics showed two transitions (**Table S3**). One was from the HOMO-1 orbit to the LUMO (oscillator strength $f_{(HOMO-1)-LUMO}$ being 0.57001) with λ_{abs} = 411.26 nm. The other was from the HOMO-2 orbit to the LUMO+1 (oscillator strength $f_{(HOMO-2)-(LUMO+1)}$ being 0.6166) with λ_{abs} = 300.35 nm. The results of theoretical calculation fitted the experimental data of the linear absorption.
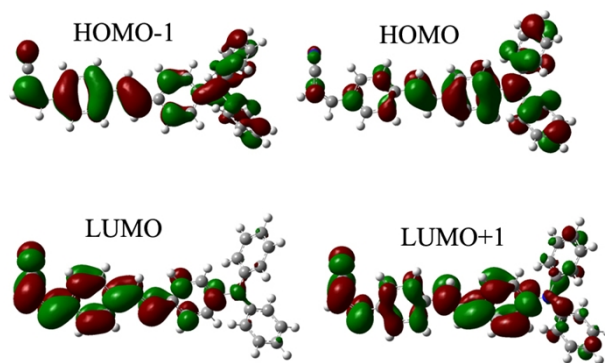
Figure S16 Calculated frontier orbital of **L** in the gas phase

Table S3 Some of calculated excitation energies (E), oscillator strengths (f), corresponding wavelengths (λ_{abs} and λ_{em}) and major contributors for **L**

| E (eV)	λ (nm)	f	composition (C)	
3.0147*	411.26	0.9372	104(H-1)→106(L)	(0.36148)
			105(H)→107(L+1)	(0.57001)
3.2954	376.23	0.0139	105(H)→108(L+2)	(0. 64689)
4.1280*	300.35	0.0253	104(H-1)→108(L+2)	(0.61659)
4.2736	290.12	0.0008	97(H-8)→106(L)	(0.58090)

* main transition
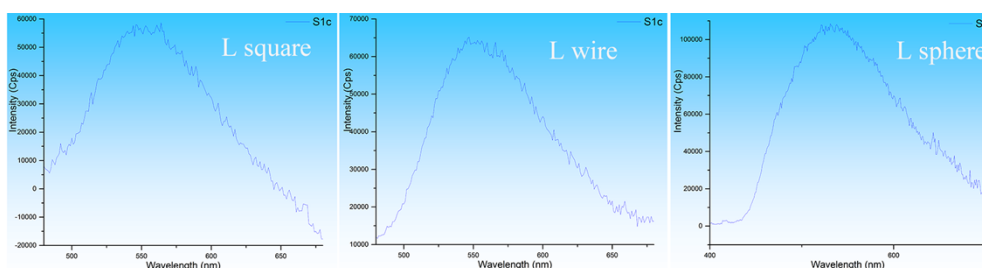
Figure S17 Fluorescence spectra of the three samples corresponding to the FL quantum yield experiment

Photostability

Photostability is an important property for the application of a probe in fluorescence microscopy as it is prolonged or repeated under irradiation [S6]. Thus, the photochemical stability of **L** square, **L** wire and **L** sphere was investigated, respectively. Measurements were carried out by recording the differences between absorbance as

a function of time as shown in **Figure S18**. Photostability is defined by time-dependent variation in absorption maxima (A/A_0) [S7] of three samples in **Figure S18d**.

As for **L** nanosquare, when the sample was irradiated for 30 min, the absorption maxima decreased for about 33%. While for **L** wire, the absorption maxima decreased for 10%, which revealed 5% decrease for **L** sphere. The results indicated that the three samples had ample photostability properties required for biological research, and that **L** wire and **L** sphere were more photostable than free **L** square. The phenomenon also revealed that the formation procrdure of free **L** square may be longer than the stabilization time of **L** wire and sphere.
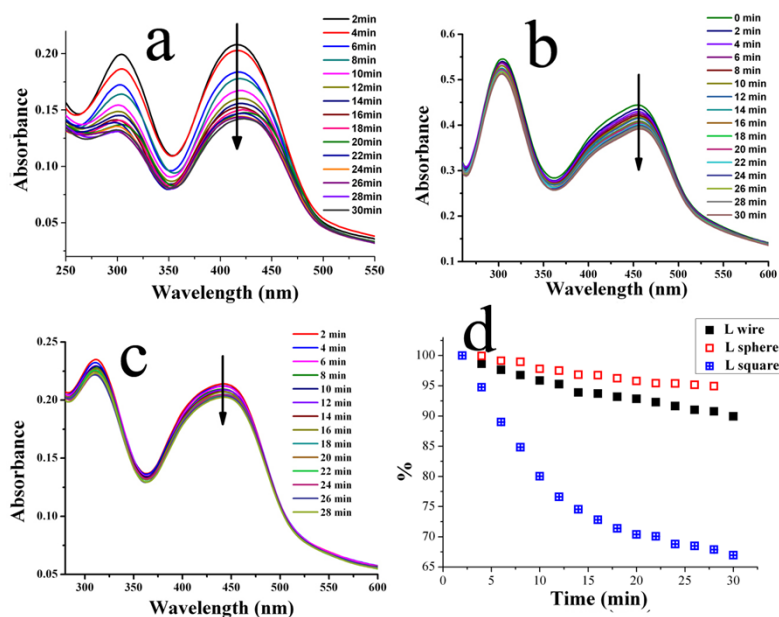

Figure S18 Kinetic changes in the absorption spectra of the corresponding samples: (a) **L** square, (b) **L** wire, (c) **L** sphere, and (d) a plot of the percentage of the absorption at the wavelengths indicated by the vertical line in a-c as a function of time for the samples.

Thermostability

Except for photostability, thermal stability is also a key character of a sample, because it will often be heated, e.g., in an incubator, even though experimental temperatures used for cell culture, cell incubation and/or 2PFM imaging are not typically very high.

Thermostability test of **L** at three states was performed using thermogravimetic analysis (TGA) (**Figure S19**). **L** square exhibited high thermal stability, which lost its weight from 342 °C to 402 °C. The quickest decomposition temperature (T_{decomp}) was determined by using DTG from the measurement of the change in mass of the sample with varying temperature, which was 384 °C. The decomposition temperature of **L** wires and **L** spheres were also

larger than room temperature. The data indicated that the three samples had ample thermostability properties required for biological research.
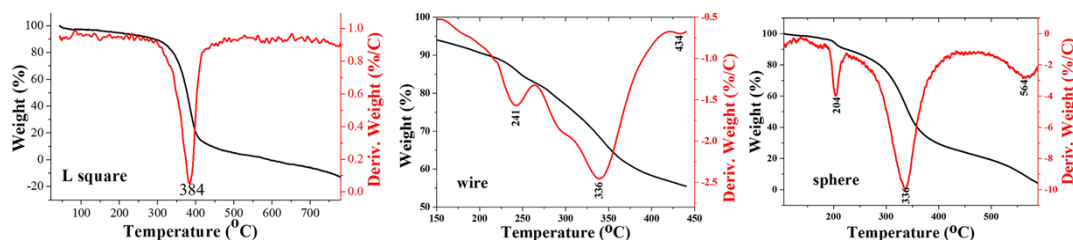

Figure S19 TG and DTG curves of a) **L** square, b) **L** wire and c) **L** sphere.

Nonlinear optical measurements

The nonlinear optical properties of the three samples were measured through Z-scan measurement and two-photo-excited fluorescence (2PEF) using femtosecond laser pulse and Ti:95 sapphire system (10 Hz, 140 fs). For 2PEF measurements, quartz-glass sample with 1.0 cm thickness were used. While for Z-scan measurements, the quartz-glass cell was 1.0 mm thick, and the average laser power was 36 mW. The optical path length for Z-scan was 5.0 cm from the sample.

As observed in linear absorption spectra, there was no linear absorption in the wavelength range 550-900 nm for the three samples, which indicated that there were no energy levels corresponding to one electron transition in this spectral range. Therefore, two-photon excited fluorescence (2PEF) was expected to appear if frequency up-converted fluorescence induced with a laser in this range appeared.
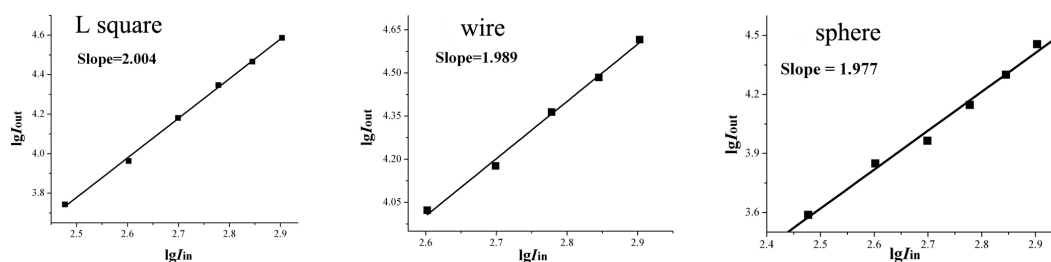
Figure S20 The logarithmic plots of the output fluorescence (I_{out}) *vs* the square of input laser power (I_{in})

To minimize the side effects of organic solvent towards live cells, these three samples were initially dissolved at a high concentration (1.0×10^{-3} mol·L^{-1}) and diluted with phosphate buffer solution to a working concentration (30 μmol·L^{-1}). Glycerol was used as a co-solvent to enhance the solubility of the samples in water. Blank test was carried out through glycerol-phosphate buffer solution.
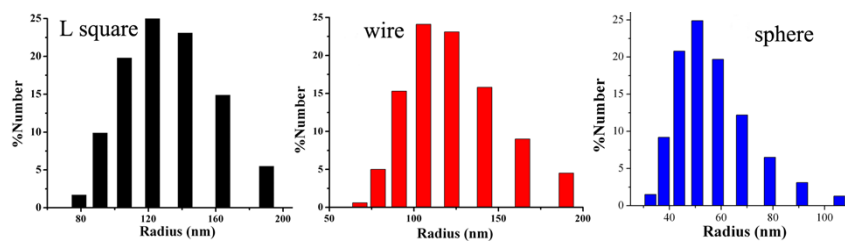
14

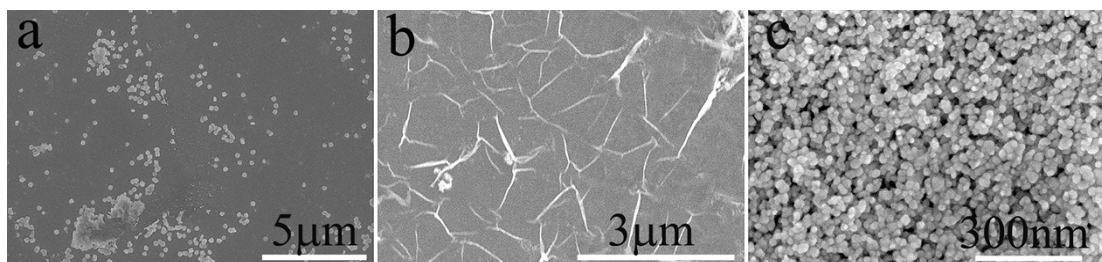**Figure S21** Size-distribution diagram of **L** square, wire and sphere, respectively.

Figure S22 SEM imaging of the upper solutions of (a) the **L** squares, (b) **L** wires and (c) **L** spheres after sonication
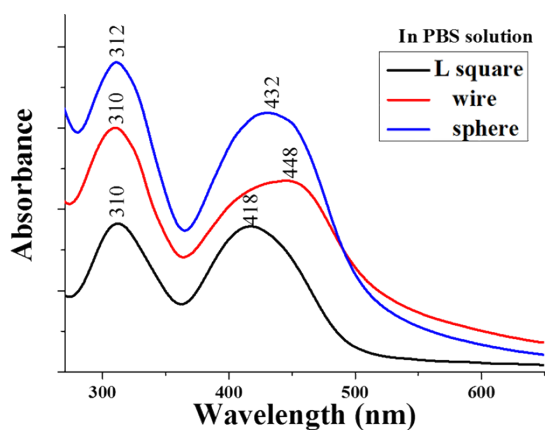

Figure S23 UV-vis spectra of **L** square, wire and sphere, respectively, in PBS solution
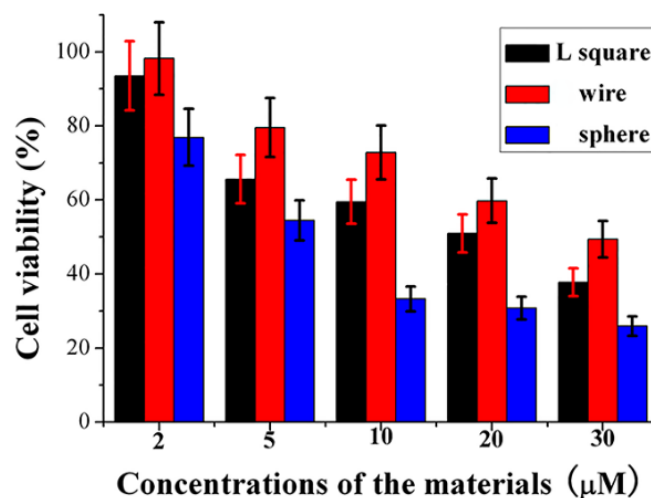

Figure S24 MTT assay of HepG2 cells treated with **L** square (black), **L** wire (red) or **L** sphere (blue) at different concentrations for 24 h.

15

MTT assay was performed to ascertain the cytotoxicity of the three samples against HepG2 cell over a 24 h period [S8]. **Fig. S24** showed that the cell viability treated with three samples at different concentrations for 24 h. The results clearly indicated that the cell viability for HepG2 cells treated with **L** wire was somewhat higher than that treated with **L** square, while it was lowered when **L** sphere was treated. The HepG2 cells incubated with 2 μM of **L** wire remained almost 100% viable after 24 h of feeding time, which was 93% when treated with **L** square and 77% for **L** sphere. The results suggested good biocompatibility of **L** aggregates at such formulation, as Cd^{2+} and Cu^{2+} are the essential trace elements in human body, and these ions with low concentration are nontoxic and/or low-toxic to human cells *in vitro*. From MTT experiment, the calculated IC_{50} value of **L** square was 20.5 μM, which was 27.6 μM for **L** wires and 7.2 μM for **L** sphere. The cytotoxicity tests showed that sub- and low-micromolar concentrations of the samples would not produce obvious toxic effects on living cells over a period of 24 h, hence the samples could safely be used for further biological studies. It is well known that Cd^{2+} is very poisonous to living cells. However, in this study, the addition of Cd^{2+} ions to the studied system did not show any influence. The reduced cytotoxicity may result from the interactions between Cd^{2+} ions and **L**, and the structure feature of **L** wire. As discussed above, the Cd^{2+} ions were embedded in **L** wires (as shown in part 3.3 and ESI† **Fig. S15**), which did not release from the structure in cell culture media (**Fig. S23, S25**). The embedded Cd^{2+} with a low concentration will not react directly to cells and may possess low poisonous.

However, it can also be observed that the IC_{50} value of **L** sphere against HepG2 cells was somewhat lower than that of the other two samples, which was also lower than that of the traditional potent antitumor platinum complex (cis-diamminedichloro-platinum (Ⅱ), CDDP) [S9]. The result indicated that **L** sphere had potential application on tumor suppressor against HepG2 cells with higher concentration. Further detailed studies on the related work were currently underway in our laboratory.

The stability of metal embedded organic nanostructures in cell media, especially whether the metal ions release from the structure, is very important before the bio-application experiments. Thus, prior to the investigations on bioimaging in living cells for the samples undertaken, the stability of the particles in living cells was studied. The fluorescence emission of the samples in the HepG2 cell media was studied. The results revealed that the relative intensity and emission band of the fluorescence were similar to that out of the cell media **(Fig. S25)**, showing the stability of the samples in the cell culture media.

To verify the results of MTT measurement, a control experiment was done. In MTT measurement, when 0.1% triton Tri-100 added into the cells, the absorbance of cells exposed to media containing DMSO/glycerol decreased sharply from 0.4863 to 0.0746, indicating the cell were killed by Tri-100 and resulting in decreasing of cell

viability. As a blank test of DMSO/glycerol solvent, the absorbance was 0.0465. When cells exposed to **L** square, **L** wire and **L** sphere (2 μmol/L), the absorbance was 0.2220, 0.4249, 0.4123, and decreased to 0.0571, 0.0553, 0.0545, respectively, after 0.1% triton incubation. The results meant that the interactions between the particles and MTT were very weak and that the MTT measurements described in the main text were credible.

Table S4. The results of MTT measurement after 0.1% triton incubation

| Material	Abs.	Material	Abs.
DMSO/glycerol	0.0465	Cell/DMSO/glycerol	0.4863
Cell/Tri100/DMSO/glycerol	0.0746		
Cell/**L square**/DMSO/glycerol	0.2220	Cell/**L square**/ Tri100/DMSO/glycerol	0.0571
Cell/**L wire**/DMSO/glycerol	0.4249	Cell/**L wire**/ Tri100/DMSO/glycerol	0.0553
Cell/**L sphere**/DMSO/glycerol	0.4123	Cell/**L sphere**/ Tri100/DMSO/glycerol	0.0545

The stability of metal embedded organic nanostructures in cell media, especially whether the metal ions release from the structure, is very important before the bio-application experiments. Thus, prior to the investigations on bioimaging in living cells for the samples undertaken, the colloidal stability of the particles was studied. The fluorescence emission of the samples was studied in cell media. The results revealed that emission band of the fluorescence were similar to that out of the cell media, with the FL intensity quenched (**Fig. S25**). The results meant that the samples were stable in the cell media.
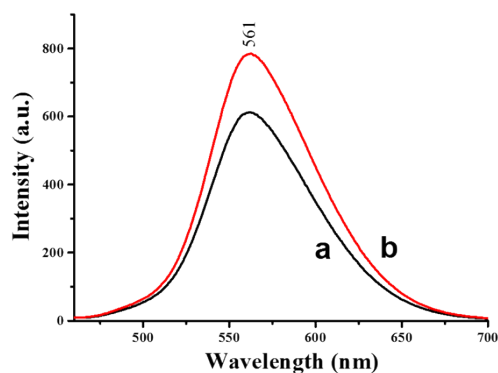
Figure S25 Fluorescence spectra of (a) **L** wire, (b) **L** sphere in HepG2 cell media
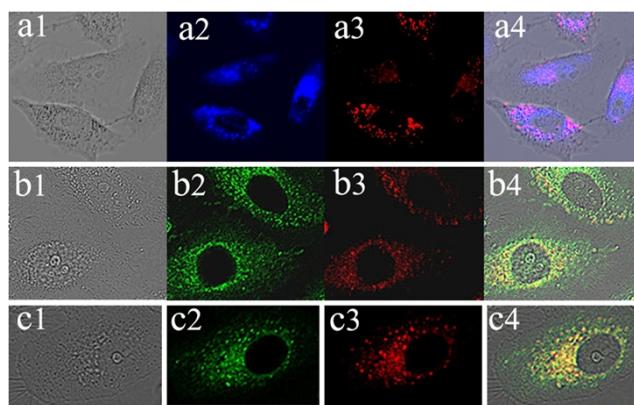
Figure S26 a) Bright-field image of HepG2 cells, b) One-photon image of HepG2 cells incubated with 20 μM **L** after 30 min of incubation, washed by PBS buffer. λ_{ex}= 457 nm (emission wavelength from 510 to 560 nm), c) Two-photon image of HepG2 cells incubated with 20 μM **L** after 30 min of incubation, washed by PBS buffer. λ_{ex} = 840 nm, d) The overlay of (a) to (c). 1) **L** square, 2) **L** wire, 3) **L** sphere.
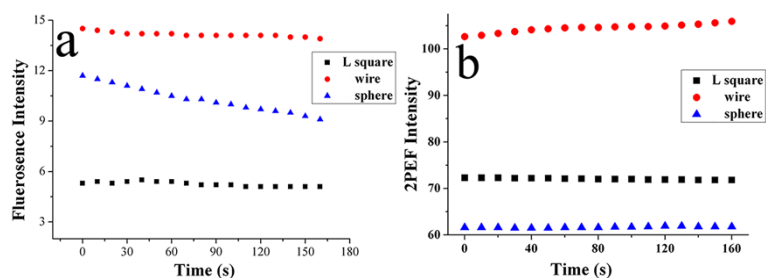
Figure S27 Time series showing a) 1PEF and b) 2PEF intensity of the samples in a HepG2 cytosol region (20 μM, 30 min) under laser exposure over 160 s.

Reference

[S1] a) J. Wang, Y. Zhao, J. Zhang, J. Zhang, B. Yang, Y. Wang, D. Zhang, H. You, D. Ma, *J. Phys. Chem. C,* **2007**, *111,* 9177-9183; b) L. Wang, Y. Zhou, J. Yan, J. Wang, J. Pei, Y. Cao, *Langmuir,* **2009**, *25,* 1306-1310.

[S2] Y. Zhou, M. Kogiso, C. He, Y. Shimizu, N. Koshizaki, T. Shimizu, *Adv. Mater.* 2007, **19**, 1055.

[S3] K. J. Wang, G. D. Li, J. X. Li, Q. Wang, J. S. Chen, *Cryst. Growth & Des.,* 2007, **7,** 2265.

[S4] M. J. G. W. T. Frisch, H. B. Schlegel, G. E. Scuseria, M. A. Robb, J. R. Cheeseman, G. Scalmani, V. Barone, B. Mennucci, G. A. Petersson, H. Nakatsuji, M. Caricato, X. Li, H. P. Hratchian, A. F. Izmaylov, J. Bloino, G. Zheng, J. L. Sonnenberg, M. Hada, M. Ehara, K. Toyota, R. Fukuda, J. Hasegawa, M. Ishida, T. Nakajima, Y. Honda, O. Kitao, H. Nakai, T. Vreven, J. A. Montgomery, Jr., J. E. Peralta, F. Ogliaro, M. Bearpark, J. J. Heyd, E. Brothers, K. N. Kudin, V. N. Staroverov, R. Kobayashi, J.

Normand, K. Raghavachari, A. Rendell, J. C. Burant, S. S. Iyengar, J. Tomasi, M. Cossi, N. Rega, J. M. Millam, M. Klene, J. E. Knox, J. B. Cross, V. Bakken, C. Adamo, J. Jaramillo, R. Gomperts, R. E. Stratmann, O. Yazyev, A. J. Austin, R. Cammi, C. Pomelli, J. W. Ochterski, R. L. Martin, K. Morokuma, V. G. Zakrzewski, G. A. Voth, P. Salvador, J. J. Dannenberg, S. Dapprich, A. D. Daniels, O. Farkas, J. B. Foresman, J. V. Ortiz, J. Cioslowski, D. J. Fox, *Gaussian 09, Revision B. 01*. Gaussian, Inc., Wallingford CT. 2009.

[S5] X. J. Zhang, X. H. Zhang, K. Zou, C. S. Lee, S. T. Lee, *J. Am. Chem. Soc.*, 2007, **129**, 3527.

[S6] a) H. Y. Ahn, S. Yao, X. H. Wang, K. D. Belfield, *ACS Appl. Mater. Interfaces* 2012, *4*, 2847; b) F. J. Song, *Photochem. Photobiol. A* 2004, **168,** 53.

[S7] a) J. R. Lakowicz, Principles of Fluorescence Spectroscopy, Springer: New York, 2006; b) M. A. Qaddoura, K. D. Belfield, P. Tongwa, J. E. DeSanto, T. V. Timofeeva, P. A. Heiney, *Supramol. Chem.,* 2011, **23**, 731.

[S8] H. Y. Ahn, K. E. Fairfull-Smith, B. J. Morrow, V. Lussini, B. Kim, M. V. Bondar, S. E. Bottle, K. D. Belfield, *J. Am. Chem. Soc.* 2012, **134**, 4721.

[S9] Y. Ohya, H. Oue, K. Nagatomi, T. Ouchi, *Biomacromolecules*, 2001, **2**, 927.